Article

Novel Red-Emitting $BaBi_2B_4O_{10}$:Eu^{3+} Phosphors: Synthesis, Crystal Structure and Luminescence

Andrey P. Shablinskii [1,*], Alexey V. Povolotskiy [2], Artem A. Yuriev [1,3], Yaroslav P. Biryukov [1], Rimma S. Bubnova [1], Margarita S. Avdontceva [3,*], Svetlana Yu. Janson [4] and Stanislav K. Filatov [3]

1 Institute of Silicate Chemistry of the Russian Academy of Sciences (ISC RAS), Makarova Emb. 2, Saint Petersburg 199034, Russia
2 Institute of Chemistry, Saint Petersburg State University, Universitetskaya Emb. 7/9, Saint Petersburg 199034, Russia
3 Institute of Earth Sciences, Saint Petersburg State University, Universitetskaya Emb. 7/9, Saint Petersburg 199034, Russia
4 The Center for Microscopy and Microanalysis, Saint Petersburg State University, Universitetskaya Emb. 7/9, Saint Petersburg 199034, Russia
* Correspondence: shablinskii.andrey@mail.ru (A.P.S.); m.avdontceva@spbu.ru (M.S.A.)

Abstract: The novel red-emitting $BaBi_{2-x}Eu_xB_4O_{10}$ (x = 0.05, 0.1, 0.2, 0.25, 0.3, 0.4, 0.5, 0.6) phosphors were obtained by a crystallization from a glass. Distribution of the Eu^{3+} ions over cation sites were refined for x = 0.1, 0.3 and 0.4 from single-crystal X-ray diffraction data. Emission and excitation spectra of the Eu^{3+}-doped $BaBi_2B_4O_{10}$ phosphors were investigated for the first time, where it was shown that characteristic lines are attributed to the intraconfigurational 4f-4f transitions. The optimal concentration for the $BaBi_{2-x}Eu_xB_4O_{10}$ phosphors is x = 0.4, after which a luminescence intensity decreases. The CIE chromaticity coordinates for the $BaBi_2B_4O_{10}$:Eu^{3+} (x = 0.4) phosphor (0.65, 0.35) are close to the NTSC standard values (0.67, 0.33) for commercial red phosphor. The obtained results show that the $BaBi_2B_4O_{10}$:Eu^{3+} phosphors are promising candidates for solid state lighting application.

Keywords: barium-bismuth borate; luminescence; crystal structure; phosphors; europium-activated phosphor; glasses

1. Introduction

Nowadays, white light-emitting diodes (wLED) are an important part of light source devices. The wLED-based devices have many advantages, such as high luminescence efficiency, environmental friendliness, long working lifetime, small size, light weight, durability, etc. [1–3] There are several ways to fabricate the wLED: (1) an exciting of single-phase yellow-emitting or mixed green- and red-emitting phosphors by a blue LED chip; (2) the exciting of red-, green- and blue-emitting phosphors by near ultraviolet LED chips; (3) a combination of red, green and blue separate monochromatic LED chips (RGB wLED) [4,5]. The fabrication of the latter ones is associated with many problems, such as high cost, complexity of fabricating, unstable aging of components, different thermal behavior, etc. [6] Generally, a commercial wLED is a combination of yellow-emitting phosphor $Y_3Al_5O_{12}$:Ce^{3+} (YAG: Ce^{3+}) with high photoluminescence quantum yield and good thermal stability with a blue diode chip. However, due to the absence of a red-light component in the emission of YAG: Ce^{3+}, this phosphor cannot be used as a source of warm white light with a high-color-rendering index and low correlated color temperature [7]. Thus, it is an actual scientific task to find novel red phosphors to solve the current problems.

Hence, borates activated with rare earth elements are of a great interest, and these are promising materials for the fabrication of various types of the wLED due to wide

transparency in the ultraviolet range, relatively easy synthesis, high optical damage threshold and thermal stability, and environmental friendliness in comparison to commercial red-emitting phosphors such as $(Sr, Ca)S:Eu^{2+}$, $Y_2O_2S:Eu^{3+}$ and other.

Complex compounds in the $MO–Bi_2O_3–B_2O_3$ (M = Ca, Sr, Ba) borate systems are actively studied in order to obtain promising optical matrices and materials. For example, structurally similar $MBi_2B_2O_7$ (M = Ca, Sr, Ba) [8–11] borates form a family of prospective red-emitting phosphors. The photoluminescence properties of the $M_3Bi_2(BO_3)_4:Eu^{3+}$ (M = Sr, Ba) compounds were investigated in [12,13], and the crystal structure and photoluminescence of $CaBi_2B_4O_{10}:Eu^{3+}$ phosphors were studied in [14]. Optical, structural, dielectric and photoluminescence properties of $MO–Bi_2O_3–B_2O_3$ (M = Ca, Sr, Ba) glasses were studied in [15–23].

The crystal structure of $BaBi_2B_2O_7$ contains three crystallographically independent sites for the Ba and Bi atoms. These sites split on the Bi and Ba subpositions. The average distance between centers of photoluminescence in the $BaBi_{1.60}Eu_{0.40}B_2O_7$ sample with optimal concentration is 21.7 Å [11]. The crystal structure of $Ba_3Bi_2(BO_3)_4$ also contains three disordered independent sites for the Ba and Bi atoms. Initially, the Eu^{3+} ions occupy the $M2$ site only. The concentration quenching occurs when the Eu^{3+} ions start to distribute over all three cation sites in the $Ba_3Bi_2(BO_3)_4:Eu^{3+}$ phosphor. The critical distance in the $Ba_3BiEu(BO_3)_4$ sample with optimal concentration is 9.5 Å. In the $Ba_3Bi(B_3O_6)_3$-$Ba_3Eu(B_3O_6)_3$ series of phosphors, the concentration quenching does not occur due to the large distance between the Bi(Eu) sites of about 7.2 Å [24].

This paper reports on the synthesis of the novel red-emitting $BaBi_2B_4O_{10}:Eu^{3+}$ phosphors and glasses, its crystal structure refinement from single-crystal X-ray diffraction data, and investigation of its luminescent properties.

2. Materials and Methods

The $BaBi_{2-x}Eu_xB_4O_{10}$ phosphors (x = 0, 0.05, 0.1, 0.2, 0.25, 0.3, 0.4, 0.5, 0.6) were obtained by high-temperature solid phase synthesis. Barium carbonate $BaCO_3$ (Neva Reaktiv, 99.90% purity), boric acid H_3BO_3 (Neva Reaktiv, 99.90% purity), bismuth oxide Bi_2O_3 (Neva Reaktiv, 99.90% purity) and europium oxide Eu_2O_3 (Kyrgyz CMC, 99.93% purity) were mixed in stoichiometric proportions. Initially, Eu_2O_3 was heated at 900 °C for 3 h, $BaCO_3$ and Bi_2O_3—at 600 °C for 10 h. The powders were ground in an agate mortar for 1 h. Then the powders were pressed into pellets using a LabTools hydraulic press at a pressure of 80 kg/cm^2. The pellets were placed on platinum crucibles and melted in the Nabertherm HTC furnace at 900 °C for 1 h. The melts were poured out onto a cold steel plate. As a result, the $BaBi_{2-x}Eu_xB_4O_{10}$ glasses were obtained (Figure 1). The polycrystalline samples were obtained by a crystallization of the glasses at 600 °C for 15 h.

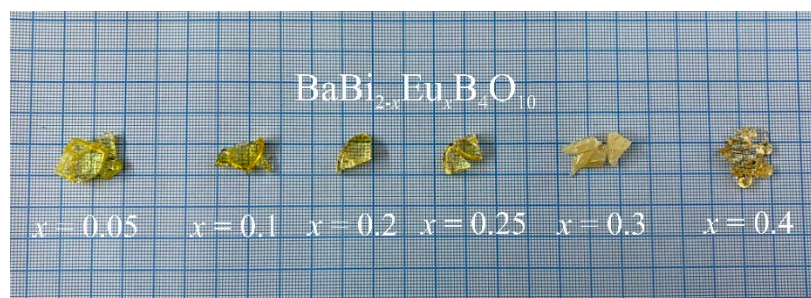**Figure 1.** The $BaBi_{2-x}Eu_xB_4O_{10}$ glasses (x = 0.05–0.4).

Powder diffraction data of the $BaBi_{2-x}Eu_xB_4O_{10}$ (x = 0–0.6) were collected using a Rigaku MiniFlex II diffractometer ($CuK\alpha$, 2θ = 10–70°, step 0.02°). The phase composition was determined using PDXL integrated X-ray powder diffraction software and PDF-2 2016 (ICDD) database.

The distribution of the Eu^{3+} ions through the crystallographic sites was studied by means of Rigaku XtaLab Synergy-S diffractometer equipped with high-speed direct-action detector HyPix-6000HE (microfocus monochromatic MoKα radiation (λ = 0.71073 Å), frame widths 1.0° in ω). The optical microscope was used for single crystal selection of the BaBi$_{2-x}$Eu$_x$B$_4$O$_{10}$ (x = 0.1, 0.3, 0.4) phosphors. Then the crystals were fixed on cryoloops with a Paratone-N oil. The obtained data was analyzed using the CrysAlisPro software (2015).

An absorption correction was introduced using the SCALE3 ABSPACK algorithm. The crystal structures of the BaBi$_{2-x}$Eu$_x$B$_4$O$_{10}$ (x = 0.1, 0.3, 0.4) phosphors were refined in the $P2_1/c$ space group using JANA2006 program [25]. Crystallographic data and refined parameters are given in Table 1, atomic coordinates, equivalent displacement parameters, atomic anisotropic displacement parameters and selected bond lengths are given in Tables S1–S3. Further details of the crystal structure investigations can be obtained from the Cambridge Structural Database on quoting the depository numbers CSD 2222018, 2222019 and 2222020.

Table 1. Crystal data, data collection and details of refinement of the BaBi$_{2-x}$Eu$_x$B$_4$O$_{10}$ (x = 0.1, 0.3, 0.4) phosphors.

Formula	BaBi$_2$B$_4$O$_{10}$ [26]	BaBi$_{1.94}$Eu$_{0.06}$B$_4$O$_{10}$	BaBi$_{1.67}$Eu$_{0.33}$B$_4$O$_{10}$	BaBi$_{1.57}$Eu$_{0.43}$B$_4$O$_{10}$
Crystal system, space group	Monoclinic $P2_1/c$			
T (K)	293			
a (Å)	10.150 (2)	10.1897(4)	10.2051 (6)	10.2360 (6)
b (Å)	6.362 (1)	6.3806 (2)	6.3872 (2)	6.3962 (4)
c (Å)	12.485 (2)	12.4469 (5)	12.4369 (5)	12.3912 (8)
β (°)	102.87 (1)	102.706 (4)	102.597 (6)	102.424 (6)
V (Å^3)	786.0 (2)	789.44 (5)	791.15 (7)	792.27 (9)
Z	4			
Radiation type	Mo $K\alpha$			
μ (mm^{-1})	49.67	48.63	44.65	43.17
Crystal size (mm)	0.14 × 0.08 × 0.06	0.04 × 0.04 × 0.1	0.08 × 0.06 × 0.04	0.06 × 0.04 × 0.02
Data collection				
Diffracto-meter	Stoe IPDS II	Rigaku XtaLab Synergy-S		
Absorption correction	multi-scan			
No. of measured, independent and observed [$I > 3\sigma(I)$] reflections	6949/2109/1813	8837/2701/1954	7448/2601/1758	8343/2681/2083
R_{int}	0.057	0.045	0.047	0.032
$(\sin\theta/\lambda)_{\text{max}}$ (Å^{-1})		0.776	0.769	0.777
Refinement				
R (obs), wR (obs), S	0.049, 0.113, 1.14	0.032, 0.033, 1.13	0.034, 0.035, 1.12	0.027, 0.030, 1.22
No. of reflections	2109	2701	2601	2681
No. of parameters	83	150	156	156
$\Delta\rho_{\text{max}}$, $\Delta\rho_{\text{min}}$ (e Å^{-3})	-	2.04/$-$1.68	2.29/$-$1.87	2.05/$-$1.39

The chemical composition (5) was studied using a QUANTA 200 3D electron microprobe equipped with an energy-dispersive spectroscopy system, operated at 16 kV and

780 pA, with a beam size of 1 μ. Analytical results are given in Table S4. The empirical formulae calculated on the basis of 10 O atoms per formula unit are $Ba_{1.01}Bi_{1.58}Eu_{0.40}B_{4.02}O_{10}$ ($x = 0.4$) and $Ba_{0.98}Bi_{1.90}Eu_{0.10}B_{4.01}O_{10}$ ($x = 0.1$).

Raman spectra were measured using Horiba LabRam HR800 spectrometer with a spectral resolution 3 cm^{-1} at 488 nm excitation. The laser beam was focused on the sample surface with 50× objective; the scattered light was collected four times for 1 min for each spectrum.

Absorption spectra were measured using a PerkinElmer Lambda 1050 spectrophotometer in a 150 mm integrating sphere with spectral resolution of 1 nm. Polycrystalline $BaSO_4$ powder was used as a reference sample.

The luminescence excitation and emission spectra as well as kinetic curves luminescence quantum yields were measured on a Horiba Fluorolog-3 spectrometer. A Horiba LabRam HR800 spectrometer equipped with confocal microscope was used to correctly compare the efficiency of photoluminescence in glasses and crystalline samples. The emission spectra were obtained using a 50× objective, which allows the excitation light to be focused into a focal region with a diameter of 2 μm. Thus, the emission spectra were measured from the same volume of glass or crystalline samples under other equal experimental conditions.

3. Results and Discussion

3.1. Powder X-ray Diffraction of the $BaBi_{2-x}Eu_xB_4O_{10}$ ($x = 0$–0.6)

X-ray phase analysis revealed that the polycrystalline samples of $BaBi_{2-x}Eu_xB_4O_{10}$ ($x = 0$–0.3) were homogenous. The sample with $x = 0.4$ contained in its phase composition $BaBi_2B_2O_7$ and/or $BaBi2-xEuxB_2O_7$ as an impurity in a quantity of about 30 wt.% (see Figure 2), which is due to a limitation of the $Eu^{3+} \rightarrow Bi^{3+}$ isomorphic substitution for these solid solutions. This leads to the area of immiscibility for the $0.3 \leq x \leq 0.4$ samples. The sample with $x = 0.5$ contains of about 18 wt.% of $Ba(Bi,Eu)_2B_4O_{10}$, 36 wt.% of $Ba_3(Bi,Eu)B_9O_{18}$, 24 wt.% of $(Bi,Eu)_4B_2O_9$ and 22 wt.% of $EuBO_3$ ($P6_3/mmc$), and the sample with $x = 0.6$ contains 11 wt.% of $Ba(Bi,Eu)_2B_4O_{10}$, 36 wt.% of $Ba_3(Bi,Eu)B_9O_{18}$, 31 wt.% $(Bi,Eu)_4B_2O_9$ and 22 wt.% of $EuBO_3$ ($P6_3/mmc$).

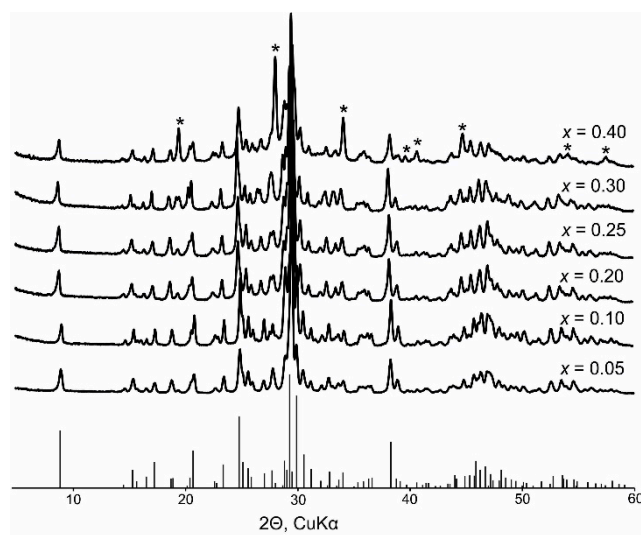**Figure 2.** Powder X-ray diffraction patterns of the $BaBi_{2-x}Eu_xB_4O_{10}$ ($x = 0.05$–0.4) phosphors. Asterisks (*) mark the $BaBi_2B_2O_7$ impurity in the $x = 0.4$ sample.

Figure 3 shows the unit cell parameters and volume vs. the Eu^{3+} concentration. This dependence can be approximated by a linear function, but a slight bend can be noticed. Perhaps this is due to the fact that, with an increase in the europium content, the Eu^{3+} ions can replace Bi^{3+} in nonequivalent crystallographic sites. It can be also assumed that as

the amount of the europium increases, the Eu^{3+} ions can replace the Bi^{3+} ones in different crystallographic sites.
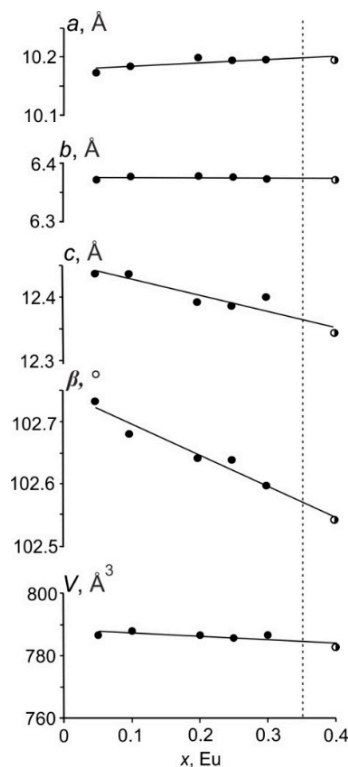

Figure 3. Dependence of unit cell parameters and volume vs. europium $x(Eu^{3+})$ concentration in the $BaBi_{2-x}Eu_xB_4O_{10}$ ($x = 0.05–0.4$) phosphors. Black-white circles indicate the two-phase sample ($x = 0.4$).

3.2. Crystal Structure of the $BaBi_{2-x}Eu_xB_4O_{10}$ ($x = 0.1, 0.3, 0.4$) Phosphors

The $BaBi_2B_4O_{10}:Eu^{3+}$ phosphors crystallize in the $BaBi_2B_4O_{10}$ structure type, monoclinic system, space group $P2_1/c$, Z = 4 (Figure 4a) [26]. Refined formulae of the $BaBi_{1.94}Eu_{0.06}B_4O_{10}$, $BaBi_{1.67}Eu_{0.33}B_4O_{10}$ and $BaBi_{1.57}Eu_{0.43}B_4O_{10}$ crystal structures are close to the $BaBi_{1.90}Eu_{0.10}B_4O_{10}$, $BaBi_{1.70}Eu_{0.30}B_4O_{10}$ and $BaBi_{1.60}Eu_{0.40}B_4O_{10}$ (5, 15, 20 at % Eu) stoichiometric mixtures. There are one Ba, two Bi, four B and ten O sites in asymmetric unit (Tables S1 and S2). The B(1), B(3) and B(4) atoms are surrounded by four oxygen atoms to form tetrahedra with bond lengths that vary in the range 1.44–1.51, 1.46–1.59, 1.44–1.51 Å (for $x = 0.1$), 1.44–1.51, 1.45–1.56, 1.45–1.51 Å ($x = 0.3$) and 1.44–1.50, 1.44–1.62, 1.44–1.50 Å ($x = 0.4$) (Table S3). The B(2) atom is triangularly coordinated by oxygen atoms and the B–O bonds are in the range 1.36–1.41 Å (for $x = 0.1$), 1.35–1.40 Å ($x = 0.3$) and 1.34–1.40 Å ($x = 0.4$). cm^{-1}.

According to [26], corner-sharing borate polyhedra form the $[B_4O_{10}]^{8-}$ chain consisting of triborate group and single BO_3 triangle. The triborate group is formed by three independent tetrahedra $B(1)O_4$, $B(3)O_4$ and $B(4)O_4$. This group can be written as <3□> in accordance with notation of Burns et al. [27]. The full notation of the $[B_4O_{10}]^{8-}$ borate polyanion is 4B:Δ3□:<3□>Δ (Figure 4b). Such a borate polyanion is unique because it was found only in the $BaBi_2B_4O_{10}$ structure type.

The Bi(1) and Bi(2) atoms form four short Bi–O bonds in the range 2.14–2.41 Å, and three and two relatively long bonds (2.56–2.87 and 2.59–2.89 Å, respectively). It results in the formation of the BiO_7 and BiO_6 polyhedra with [4+3] and [4+2] coordinations of Bi. Such a coordination of the Bi atoms is asymmetric due to the presence of the $6s^2$ stereoactive lone electron pair. The $Bi(1)O_7$ and $Bi(2)O_6$ polyhedra share edges to form the $[Bi_2O_{10}]$ dimers. These dimers are linked through the O(5) atoms to form $[Bi_2O_7]$ chains along the [010] direction [26] (Figure 4c). The Bi–O chains share edges (O3), forming $[Bi_2O_5]$

bismuthate layers in *bc* plane. The Ba(1) site has an eightfold coordination (Figure 4d) with the Ba–O bond lengths vary in the range 2.75–2.90 Å (*x* = 0.1), 2.75–2.91 Å (*x* = 0.3) and 2.74–2.89 Å (*x* = 0.4). The next four bonds are in the range 3.10–3.20 Å.
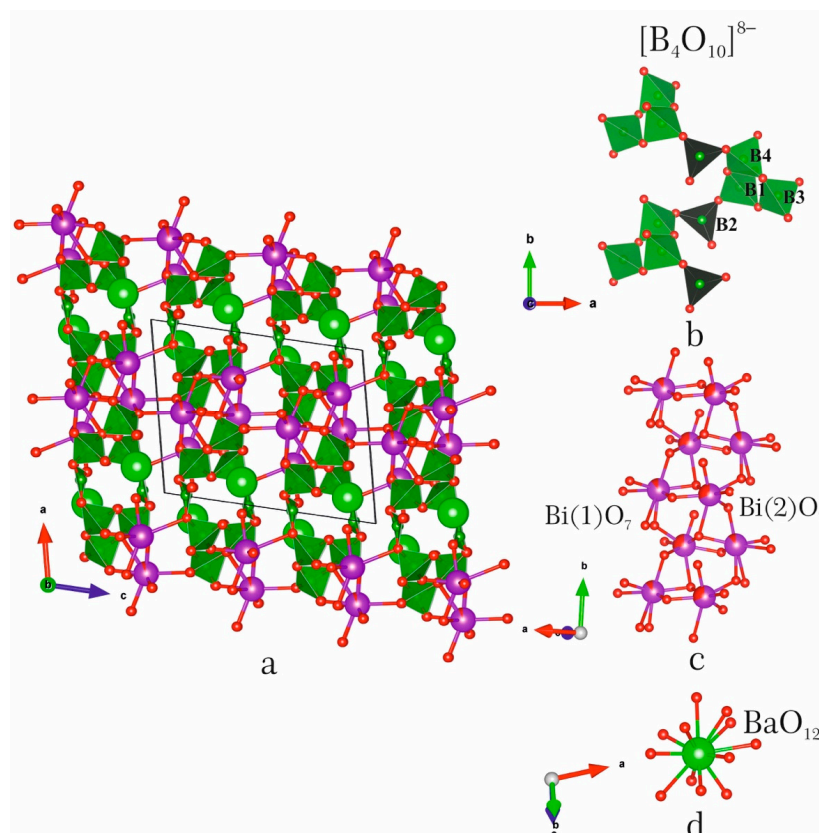

Figure 4. Structural fragments and crystal structure of $BaBi_{1.90}Eu_{0.10}B_4O_{10}$ (**a**): (**b**)—$[B_4O_{10}]$ chain, (**c**)—$[Bi_2O_7]$ chain, (**d**)—BaO_{12}.

Generally, the lone electron pair of the Bi^{3+} ion is stereoactive if the Lewis basicity strength presents in a crystal structure. In the $BaBi_2B_4O_{10}$ crystal structure, the unique borate anion $[B_4O_{10}]^{8-}$ is a structural unit. A knowledge of coordination numbers of cations and anions in a structural unit lets us calculate the Lewis basicity of the unit [27–31]. In the $[B_4O_{10}]^{8-}$ structural unit, the average coordination number of the O atoms is 3.9. There are 39 bonds in the crystal structure that involve the O atoms of the structural unit. Within the structural unit, there are 15 bonds in the BO_4 tetrahedra and BO_3 triangle. Therefore, the Lewis basicity of the structural unit is 8/24 = 0.30 *vu*. The presence of such a strong Lewis base is the determining factor for the stereoactivity of the Bi^{3+} lone electron pair. The bond-valence calculations were performed using empirical parameters taken from Brown and Altermatt (1985) [32] (Table S2).

3.3. A Distribution of the Eu^{3+} Ions over the Crystallographic Sites

The Ba and Bi cations are fully ordered in the $BaBi_2B_4O_{10}$ crystal structure [26]. In the $BaBi_{1.90}Eu_{0.10}B_4O_{10}$ crystal structure, the Eu^{3+} atoms occupy only the Bi(1) site. Then, the Eu^{3+} atoms occupy 22% of the Bi(1) site and 11% of the Bi(2) site in the $BaBi_{1.70}Eu_{0.30}B_4O_{10}$ crystal structure, and 31% of the Bi(1) site and 11% of the Bi(2) site in the $BaBi_{1.60}Eu_{0.40}B_4O_{10}$ crystal structure, respectively (Figure 5).

The immiscibility of the $BaBi_{2-x}Eu_xB_4O_{10}$ solid solutions may be caused by structural distortions. Presumably, a main reason for structural distortions is a five-fold coordination of the O(2) atom by the B(1), B(3), Bi(1), Bi(2) and Ba(1) ones. The B(1)–O(2) and B(3)–O(2) bond lengths are 1.49 and 1.56 Å in $BaBi_2B_4O_{10}$, and 1.50 and 1.62 Å in $BaBi_{1.60}Eu_{0.40}B_4O_{10}$. Usually, the B–O bond lengths in the BO_4 tetrahedron vary in the

range 1.462–1.512 Å [33]. Perhaps, the longest B–O bond (1.69 Å) was found in the crystal structure of high boracite [34], where the one O site is surrounded by four B ones. The $Bi(1)$–$O(2)$ and $Bi(2)$–$O(2)$ bond lengths are 2.73 and 2.59 Å in $BaBi_2B_4O_{10}$. The Eu atoms substitute the Bi ones in the $Bi(1)$ and $Bi(2)$ sites. The ionic radius of the Eu^{3+} ion (1.15 Å) is smaller than the Bi^{3+} one (1.24 Å) for the coordination number equals 7 [35]. Therefore, in the $BaBi_{1.60}Eu_{0.40}B_4O_{10}$ crystal structure, the $Bi(1)$–$O(2)$ and $Bi(2)$–$O(2)$ bond lengths are shorter (2.66 and 2.60 Å). The $Ba(1)$–$O(2)$ bond practically does not change (see Table S2). Apparently, these structural distortions are caused by the $Eu^{3+} \rightarrow Bi^{3+}$ substitution. The bond valence of the $B(1)$–$O(2)$ bond decreases from 0.60 *vu* in in $BaBi_2B_4O_{10}$ to 0.50 *vu* in $BaBi_{1.60}Eu_{0.40}B_4O_{10}$. Such a decrease is partially compensated by an increase in the valence of the $Bi(1)$–$O(2)$ bond from 0.18 to 0.21 *vu*. The bond valence sum for the $O(2)$ site decreases from 1.97 to 1.87 *vu*. Presumably, this is one of the reasons leading to the immiscibility of the $BaBi_{2-x}Eu_xB_4O_{10}$ solid solutions.
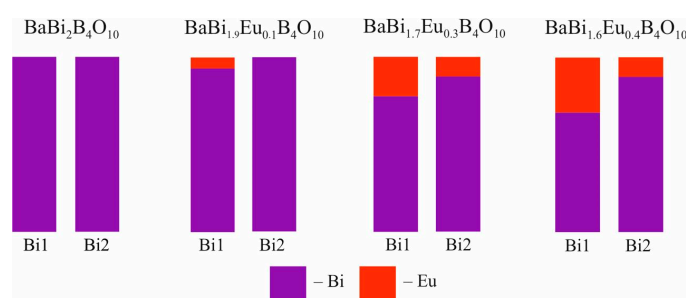

Figure 5. Occupation (%) of the crystallographic sites in the $BaBi_{2-x}Eu_xB_4O_{10}$ (x = 0, 0.1, 0.3, 0.4) crystal structures. Data for $BaBi_2B_4O_{10}$ are given in [26].

3.4. Raman Spectroscopy

The Raman spectra of the samples are shown in Figure 6. According to the spectra, the structure of the samples does not change up to when the Eu^{3+} concentration equals 0.30. A further increase in the concentration of the activator ion leads to the area of immiscibility of the $BaBi_{2-x}Eu_xB_4O_{10}$ solid solutions. The sample with x = 0.4 contained about 70 wt.%, $BaBi_{2-x}Eu_xB_4O_{10}$ and 30 wt.% $BaBi_2B_2O_7$ and/or $BaBi_{2-x}Eu_xB_2O_7$ in its phase composition. The samples with x = 0.5 and 0.6 have difficult phase compositions (see Section 3.1). With an increase in the Eu content, the concentration of phases ($Ba_3(Bi,Eu)B_9O_{18}$ and $(Bi,Eu)_4B_2O_9$) containing only the BO_3 triangular radicals also increases. Broad Raman bands confirm a disordered model of the crystal structure. The main structural units are the BO_4 tetrahedra and the BO_3 triangles.
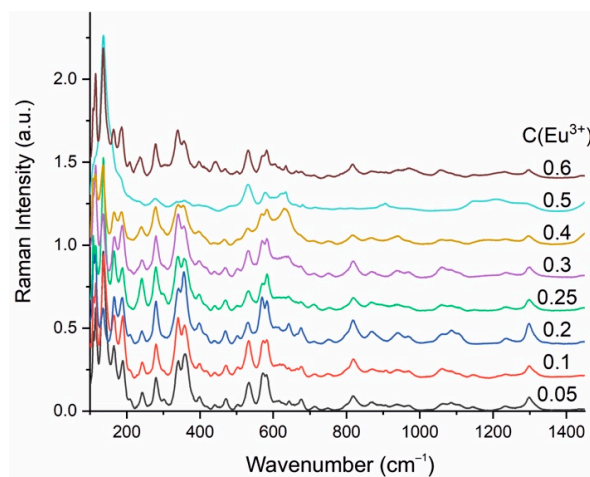

Figure 6. Raman spectra of the $BaBi_{2-x}Eu_xB_4O_{10}$ (x = 0.05–0.6) samples (the x = 0.05–0.6 concentrations are shown by different color).

Assignment of the Raman bands is presented in Table 2. Due to the combination of one BO_3 and three crystallographic independent BO_4 units consisting the $[B_4O_{10}]^{8-}$ chain, the more detailed assignment of the vibrations is difficult. The positions of the Raman bands are assigned in accordance with [36,37].

Table 2. Raman bands assignment for the $BaBi_{2-x}Eu_xB_4O_{10}$ (x = 0–0.6) samples.

Raman Band, cm^{-1}	Assignment
115	Bi-O
135	Bi^{3+} cations in the form of (BiO_6)
165	δ (BO_4)
188, 242, 280	$\gamma(BO_3)$
341	δ $(BO_4)/\gamma(BO_3)$
358	δ $(BO_3)/\gamma(BO_3)$
397, 470	Bi–O–Bi bond vibrations of BiO_6 octahedral
534, 569	δ $(BO_3)/\delta(BO_4)$
582	Stretching vibrations of Bi–O bonds in BiO_6 octahedrons
642, 676	$\delta(BO_4)/\gamma(BO_3)$
817, 869,	ν_s (BO_4)
940	ν_s (BO_3)
968	ν_s (BO_4)
1060, 1086, 1105	ν_{as} (BO_4)
1234, 1298	ν_{as} (BO_3)

ν—stretching vibration, δ—bending vibration, γ—librational vibration, s—symmetrical.

3.5. Absorption Spectroscopy

The absorption spectra of the $BaBi_{2-x}Eu_xB_4O_{10}$ (x = 0–0.6) samples (Figure 7a) demonstrate that the blue edge of the optical transparency window is below 400 nm. Narrow peaks correspond to the transitions between electronic states of Eu^{3+} ions. The position of the fundamental absorption edge plotted in Tauc coordinates was used to determine the optical band gap. The obtained values of the optical band gap depending on the concentration of active ions are shown in Figure 7b. The decrease in the band gap may be due to the occurrence of the immiscibility area between the $0.3 \leq x \leq 0.4$ samples and the formation of defective localized states in the band gap at high concentrations of europium ions.
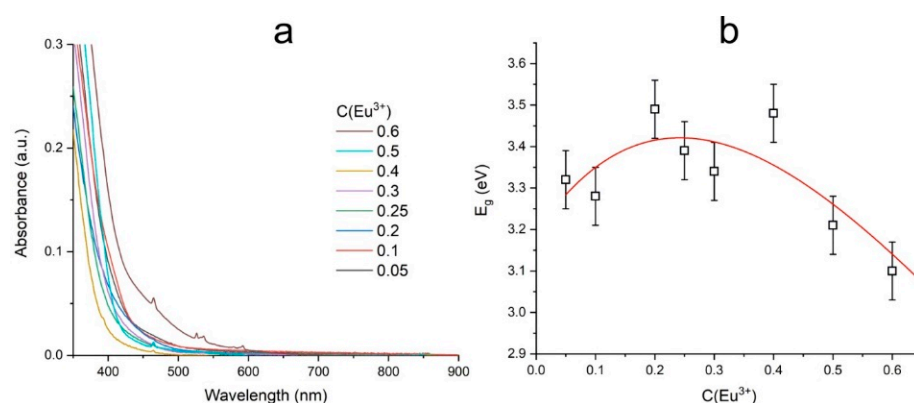

Figure 7. UV-Vis absorption spectra (**a**) and dependence of bandgap energy on Eu^{3+} concentration (**b**) in the $BaBi_{2-x}Eu_xB_4O_{10}$ (x = 0–0.6) crystalline samples.

3.6. Photoluminescence Properties

All narrow bands in the luminescence excitation spectra correspond to the f-f transitions of the Eu^{3+} ions (Figure 8a). The broad band to the left of 350 nm is a charge transfer band which corresponds to the electronic transitions from 2p orbitals of O^{2-} to 4f orbitals of the Eu^{3+} ions [10.1016/j.jlumin.2013.10.002]. It can be seen that the optimal pump wavelength for the $BaBi_{2-x}Eu_xB_4O_{10}$ (x = 0–0.6) samples is 392 nm, which corre-

sponds to the $^7F_0$-$^5L_6$ transition of the Eu^{3+} ions. Therefore, all experiments of the studied samples' luminescent properties were carried out at 392 nm excitation. Figure 8b shows the luminescence spectra of the $BaBi_{2-x}Eu_xB_4O_{10}$ ($x = 0$–0.6) samples depending on the europium ions concentration.

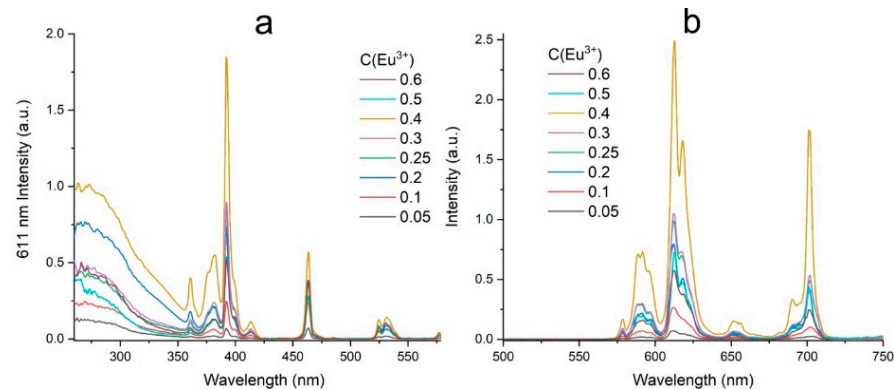**Figure 8.** Excitation spectra of 611 nm luminescence band (**a**); photoluminescence spectra at 392 nm excitation (**b**).

To determine the optimal concentration of active ions, the integrated intensity of the luminescence spectra was compared. The obtained concentration dependence of the integral intensity of Eu^{3+} ions is shown in Figure 9a. Obviously, the optimal concentration of the europium ions in the samples under study is $x = 0.4$. With a further increase in the concentration, the luminescence intensity decreases due to the concentration quenching and area of the immiscibility of the solid solution. The quantum yield measured for the $x = 0.4$ sample is 10% (Figure 9b).
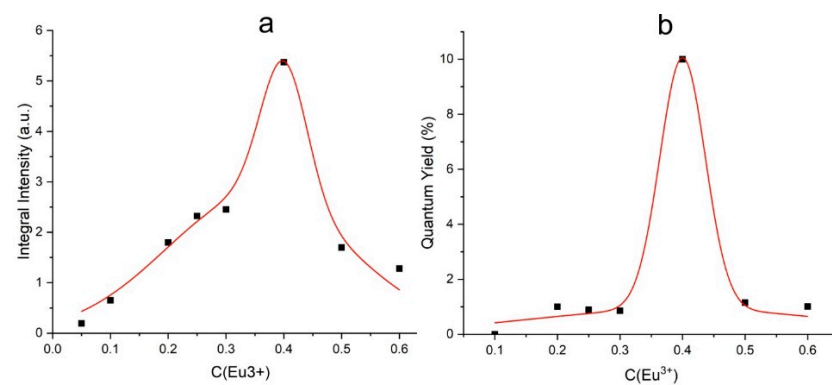

Figure 9. Dependence of the photoluminescence integral intensity on Eu^{3+} concentration (**a**); quantum yield of the $BaBi_{2-x}Eu_xB_4O_{10}$ ($x = 0$–0.6) samples (**b**).

All luminescence kinetic curves fit well with a single-exponential function (Figure 10a). One of the parameters sensitive to the environment of the active ions is the lifetime of excited states. The figure shows the dependence of the lifetime of the $^5D_0$ level on the concentration of the Eu^{3+} ions (Figure 10b).

The photoluminescence properties of glass and polycrystalline samples were compared using a Horiba LabRam HR800 spectrometer. The comparison was carried out according to the luminescence band in the region of 700 nm. It can be seen that the band is wider in the amorphous sample than in the crystalline one (Figure 11a). To compare the luminescent properties, the integral intensities were measured. The integrated intensity of amorphous samples is higher than crystalline ones with the corresponding concentration of active ions in the entire concentration range (Figure 11b).
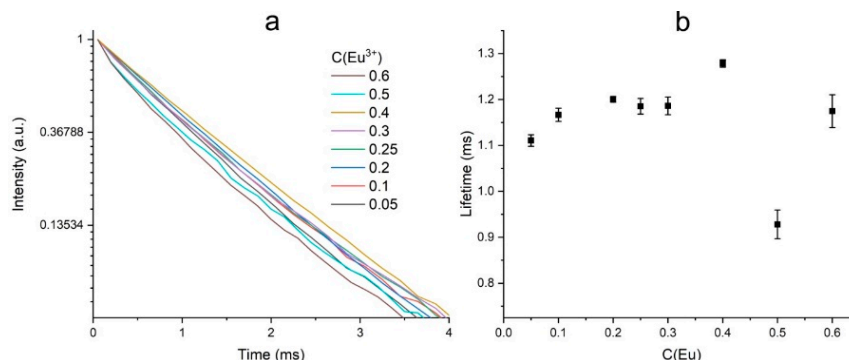
Figure 10. Photoluminescence kinetic curves in the region of the 611 nm band upon excitation at 392 nm (**a**); dependence of Eu^{3+} $^5D_0$ level lifetime on Eu^{3+} concentration (**b**).
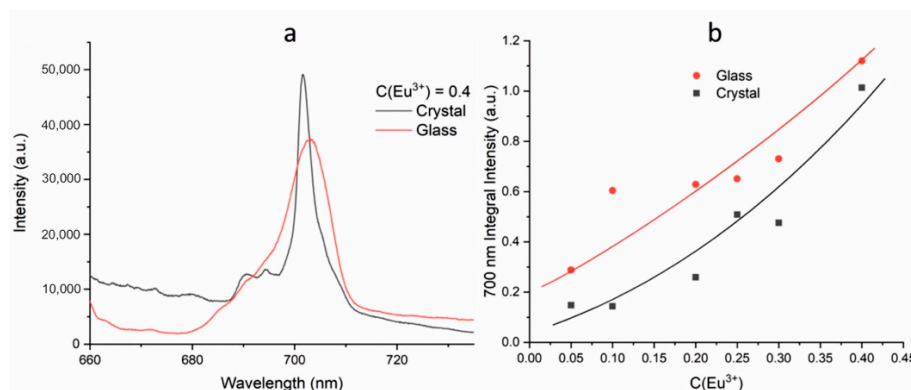

Figure 11. Luminescence spectra of glass and polycrystalline $BaBi_{2-x}Eu_xB_4O_{10}$ (x = 0–0.4) samples upon 632.8 nm excitation (**a**); integral intensity of luminescence for glass and polycrystalline $BaBi_{2-x}Eu_xB_4O_{10}$ (x = 0–0.4) samples (**b**).

The CIE chromaticity coordinates are given in Table 3 and presented in Figure 12. The CIE chromaticity coordinates for the $BaBi_{1.60}Eu_{0.40}B_4O_{10}$ phosphor at room temperature were (0.65, 0.35). This is close to the NTSC standard values (0.67, 0.33) for commercial red phosphor.

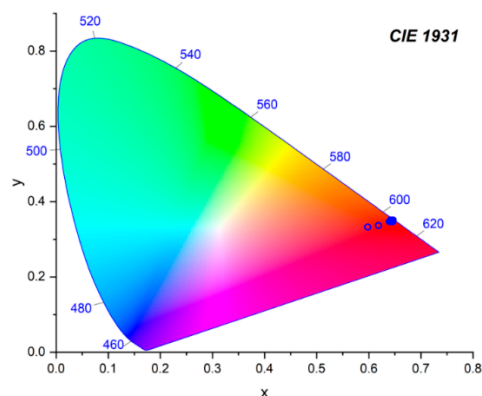**Figure 12.** CIE chromaticity coordinates of the $BaBi_{2-x}Eu_xB_4O_{10}$ (x = 0–0.6) concentration series.

Table 3. CIE (CIE 1931) chromaticity coordinates of $BaBi_{2-x}Eu_xB_4O_{10}$ (x = 0.05–0.6) samples.

C (Eu^{3+})	x	y
0.05	0.60	0.33
0.1	0.64	0.35

Table 3. *Cont.*

C (Eu^{3+})	x	y
0.2	0.64	0.35
0.25	0.64	0.35
0.3	0.64	0.35
0.4	0.65	0.35
0.5	0.62	0.34
0.6	0.65	0.35

3.7. Energy Migration

The energy transfer between luminescence centers is determined mainly by the distance between the sites occupied by the activator ions in the crystal structure. According to the Dexter's theory [38], a critical distance of 5 Å or less is necessary for achievement of the exchange interaction. Usually, the emission intensity decreases at high doping concentration and that can be explained as a result of the dipole-dipole interaction between the Eu^{3+} ions, the probability of which increases with decreasing distance between active ions. The distance between the Bi atoms in the chain is approximately 3.6 Å, and between the Bi sites from different [Bi$_2$O$_7$] chains within the layer is approximately 3.7 Å (Figure 13). The distance between the Bi sites which belong to different layers is already much greater than ~6.0 Å, which means that in this borate, with a high degree of probability, two-dimensional energy transfer between luminescence centers occurs. According to [39,40], this leads to an increase in the value of concentration quenching relative to the three-dimensional energy transfer between luminescence centers, and a decrease relative to the one-dimensional one.
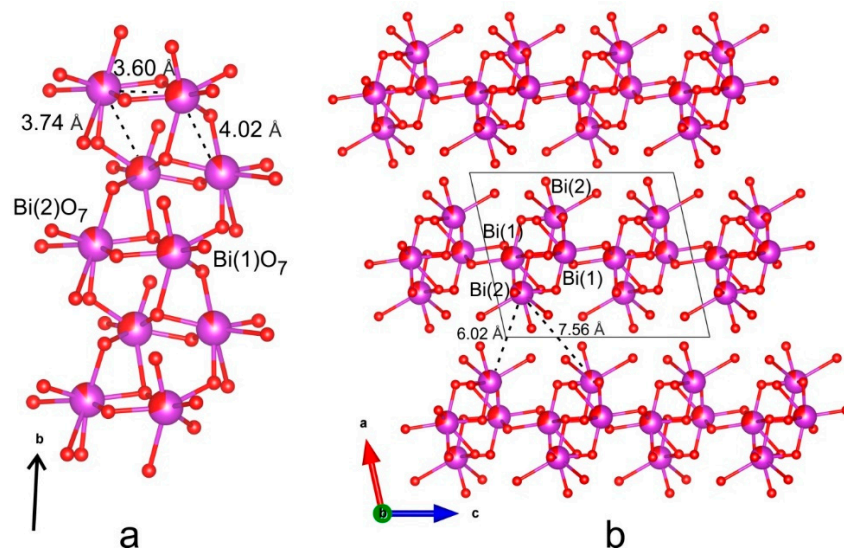

Figure 13. Bi–O chain (**a**) and Bi–O layers (**b**) in the BaBi$_{1.60}$Eu$_{0.40}$B$_4$O$_{10}$ crystal structure.

The emission intensity of these borates can be explained in terms of the area of miscibility of the BaBi$_{2-x}$Eu$_x$B$_4$O$_{10}$ solid solutions ($x = 0$–0.35) because the sample with $x = 0.4$ contains two phases (BaBi$_{2-x}$Eu$_x$B$_4$O$_{10}$ and BaBi$_2$B$_2$O$_7$ or BaBi$_{2-x}$Eu$_x$B$_2$O$_7$). Although, the optimal concentration for the BaBi$_{2-x}$Eu$_x$B$_4$O$_{10}$ phosphors is $x = 0.4$ because this sample has the highest quantum yield. Although the critical energy transfer distance R_c between the europium ions was not achieved, it seems interesting to compare the energy transfer distance for optimal concentrations. The critical energy transfer distance can be calculated using an equation proposed by [41]:

$$R_c \approx 2 \left[\frac{3V}{4\pi x_c N} \right]^{\frac{1}{3}}$$

where x_c is the critical doping content, N—the number of cation sites in the unit cell that can be occupied by activator ions and V—the volume of unit cell. Using these parameters, R_c was found to be 26.3 Å.

4. Conclusions

The novel red-emitting $BaBi_{2-x}Eu_xB_4O_{10}$ (x = 0.05, 0.1, 0.2, 0.25, 0.3, 0.4, 0.5, 0.6) phosphors were obtained by a crystallization from the glass. Crystal structures of the novel $BaBi_{2-x}Eu_xB_4O_{10}$ (x = 0.1, 0.3, 0.4) phosphors were refined. Single-crystal X-ray diffraction showed that the $Eu^{3+} \rightarrow Bi^{3+}$ isomorphic substitution does not change the monoclinic system of the solid solutions. It is shown that the Eu^{3+} atoms first occupy the Bi(1) and then start to substitute the Bi(2) sites. This leads to the existence of the area of immiscibility for the $0.3 \leq x \leq 0.4$ samples. An analysis of the distances between the luminescence centers shows that two-dimensional (2D) energy transfer can occur in these phosphors. The highest emission intensity with a quantum yield of 10% was demonstrated by $BaBi_{1.60}Eu_{0.40}B_4O_{10}$. In terms of the highest quantum yield, the optimal concentration for the $BaBi_{2-x}Eu_xB_4O_{10}$ phosphors is found to be x = 0.4. The CIE chromaticity coordinates for the $BaBi_2B_4O_{10}$:Eu^{3+} (x = 0.4) phosphor were determined to be (0.65, 0.35) which are close to those for the NTSC standard (0.67, 0.33) for commercial red phosphor.

Supplementary Materials: The following supporting information can be downloaded at: https://www.mdpi.com/article/10.3390/sym15040918/s1.

Author Contributions: Writing—original draft, A.P.S., Y.P.B., A.V.P. and A.A.Y.; Writing—review & editing, A.P.S., Y.P.B., S.K.F. and R.S.B.; Investigation, A.P.S., M.S.A., A.V.P., A.A.Y. and S.Y.J.; Project administration, A.P.S., Y.P.B. and R.S.B.; Data curation, A.P.S., R.S.B. and S.K.F.; Visualization, A.P.S. and A.A.Y.; Supervision, A.P.S. All authors have read and agreed to the published version of the manuscript.

Data Availability Statement: CCDC 2222018, 2222019 and 2222020 contain the crystallographic data for this paper. These data can be obtained free of charge via https://www.ccdc.cam.ac.uk/Community/Depositastructure/CSDCommunications/ (accessed on 25 November 2022).

Conflicts of Interest: The authors declare no conflict of interest.

References

1. Mondal, K.; Singh, D.K.; Manam, J. Spectroscopic behavior, thermal stability and temperature sensitivity of Ca_2SiO_4: Eu^{3+} red emitting phosphor for solid state lighting application. *J. Alloys Compd.* **2018**, *761*, 41–51. [CrossRef]
2. Cao, R.; Ye, Y.; Peng, Q.; Zheng, G.; Ao, H.; Fu, J.; Guo, Y.; Guo, B. Synthesis and luminescence characteristics of novel red-emitting $Ba_2TiGe_2O_8$: Mn^{4+} phosphor. *Dye. Pigment.* **2017**, *146*, 14–19. [CrossRef]
3. Zhong, J.; Xu, M.; Chen, D.; Xiao, G.; Ji, Z. Novel red-emitting Sr_2LaSbO_6: Eu^{3+} phosphor with enhanced $^5D_0 \rightarrow {}^7F_4$ transition for warm white light-emitting diodes. *Dye. Pigment.* **2017**, *146*, 272–278. [CrossRef]
4. Hu, G.; Hu, X.; Chen, W.; Cheng, Y.; Liu, Z.; Zhang, Y.; Liang, X.; Xiang, W. Luminescence properties and thermal stability of red phosphor Mg_2TiO_4: Mn^{4+} additional Zn^{2+} sensitization for warm W-LEDs. *Mater. Res. Bull.* **2017**, *95*, 277–284. [CrossRef]
5. Huang, X. Solid-state lighting: Red phosphor converts white LEDs. *Nat. Photonics* **2014**, *8*, 748. [CrossRef]
6. Du, P.; Bharat, L.K.; Yu, J.S. Strong red emission in Eu^{3+}/Bi^{3+} ions codoped $CaWO_4$ phosphors for white light-emitting diode and field-emission display applications. *J. Alloys Compd.* **2015**, *633*, 37–41. [CrossRef]
7. Zhu, H.; Lin, C.C.; Luo, W.; Shu, S.; Liu, Z.; Liu, Y.; Kong, J.; Ma, E.; Cao, Y.; Liu, R.-S.; et al. Highly efficient non-rare-earth red emitting phosphor for warm white light-emitting diodes. *Nat. Commun.* **2014**, *5*, 4312. [CrossRef]

8. Barbier, J.; Cranswick, L.M.D. The Non-Centrosymmetric Borate Oxides, $MBi_2B_2O_7$ (M = Ca, Sr). *J. Solid State Chem.* **2006**, *179*, 3958–3964. [CrossRef]

9. Bubnova, R.S.; Shablinskii, A.P.; Volkov, S.N.; Filatov, S.K.; Krzhizhanovskaya, M.G.; Ugolkov, V.L. Crystal Structures and Thermal Expansion of $Sr_{1−x}Ba_xBi_2B_2O_7$ Solid Solutions. *Glass Phys. Chem.* **2016**, *42*, 337–438. [CrossRef]

10. Volkov, S.; Bubnova, R.; Shorets, O.; Ugolkov, V.; Filatov, S. Crystal structure and strong uniaxial negative thermal expansion of $CaBi_2B_2O_7$ borate. *Inorg. Chem. Commun.* **2020**, *122*, 108262. [CrossRef]

11. Shablinskii, A.P.; Povolotskiy, A.V.; Kolesnikov, I.E.; Biryukov, Y.P.; Bubnova, R.S.; Avdontceva, M.S.; Demina, S.V.; Filatov, S.K. Novel red-emitting color-tunable phosphors $BaBi_{2−x}Eu_xB_2O_7$ (x = 0–0.40): Study of the crystal structure and luminescence. *J. Solid State Chem.* **2022**, *307*, 122837. [CrossRef]

12. Shablinskii, A.; Bubnova, R.; Kolesnikov, I.; Krzhizhanovskaya, M.; Povolotskiy, A.; Ugolkov, V.; Filatov, S. Novel $Sr_3Bi_2(BO_3)_4$: Eu^{3+} red phosphor: Synthesis, crystal structure, luminescent and thermal properties. *Solid State Sci.* **2017**, *70*, 93–100. [CrossRef]

13. Shablinskii, A.; Kolesnikov, I.; Bubnova, R.; Povolotskiy, A.; Lähderanta, E.; Filatov, S. A novel thermally stable $Ba_3Bi_2(BO_3)_4$: Eu^{3+} red phosphor for solid state lighting application. *J. Lumin.* **2019**, *216*, 116714. [CrossRef]

14. Shablinskii, A.P.; Povolotskiy, A.V.; Yuriev, A.A.; Bubnova, R.S.; Kolesnikov, I.E.; Filatov, S.K. Novel $CaBi_2B_4O_{10}$: Eu^{3+} red phosphor: Synthesis, crystal structure, luminescence and thermal expansion. *Solid State Sci.* **2020**, *106*, 106280. [CrossRef]

15. Tichy, L.; Ticha, H.; Herzigova, L.; Ozdanova, J. Some physical properties of $(Bi_2O_3)_x(BaO)_{0.5−x}(B_2O_3)_{0.5}$ glasses. *Mater. Chem. Phys.* **2011**, *126*, 289–294. [CrossRef]

16. Egorysheva, A.V.; Volodin, V.D.; Skorikov, V.M. Glass Formation in the Bi_2O_3–B_2O_3–BaO System. *Inorg. Mater.* **2008**, *44*, 1261–1265. [CrossRef]

17. Egorysheva, A.V.; Volodin, V.D.; Milenov, T.; Rafailov, P.; Skorikov, V.M.; Dudkina, T.D. Glass Formation in the CaO–Bi_2O_3–B_2O_3 and SrO–Bi_2O_3–B_2O_3 Systems. *Russ. J. Inorg. Chem.* **2010**, *55*, 1810–1817. [CrossRef]

18. Egorysheva, A.V.; Volodin, V.D.; Berezovskaya, I.V.; Zubar', E.V.; Skorikov, V.M.; Milenov, T.; Rafailov, P. Effect of Eu_2O_3 Doping on the Crystallization Behavior of BaO–Bi_2O_3–B_2O_3 Glasses. *Inorg. Mater.* **2012**, *48*, 948–952. [CrossRef]

19. Majhi, K.; Varma, K. Structural, dielectric and optical properties of transparent glasses and glass-ceramics of $SrBi_2B_2O_7$. *J. Non-Cryst. Solids* **2008**, *354*, 4543–4549. [CrossRef]

20. Shablinskii, A.P.; Drozdova, I.A.; Volkov, S.N.; Krzhizhanovskaya, M.G.; Bubnova, R.S. Production and study of glass ceramics in $Sr_{1−x}Ba_xBi_2B_2O_7$ system. *Fiz. I Khimiya Stekla* **2012**, *38*, 886–889.

21. Singh, V.; Kushwaha, H.S.; Vaish, R. Photocatalytic study on $SrBi_2B_2O_7$ (SrO–Bi_2O_3–B_2O_3) transparent glass ceramics. *Mater. Res. Bull.* **2018**, *99*, 453–459. [CrossRef]

22. Shablinskii, A.P.; Povolotskii, A.V.; Drozdova, I.A.; Kolesnikov, I.E.; Bubnova, R.S. New luminescent $BaBi_{2−x}Eu_xB_2O_7$ glassmaterials. *Glass Phys. Chem.* **2019**, *45*, 74–78. [CrossRef]

23. Padmaja, G.; Devarajulu, G.; Raju, B.D.P.; Turpu, G.; Srishailam, K.; Reddy, B.V.; Kumar, G.P. Synthesis of $Sr_{1−x}Ba_xBi_2B_2O_7$ glass ceramics: A study for structure and characterization using experimental techniques and DFT method. *J. Mol. Struct.* **2020**, *1220*, 128660. [CrossRef]

24. Cai, G.; Li, M.; Liu, J.; Jin, S.; Wang, W.; Zheng, F.; Chen, X. Crystal structure and $Eu(^{3+})$/$Tb(^{3+})$ doped luminescent properties of a new borate $Ba_3BiB_9O_{18}$. *Mater. Res. Bull.* **2009**, *44*, 2211–2216. [CrossRef]

25. Petříček, V.; Dušek, M.; Palatinus, L. Crystallographic Computing System JANA2006: General feature. *Z. Für Krist. Cryst. Mater.* **2014**, *229*, 345–352. [CrossRef]

26. Bubnova, R.; Krivovichev, S.; Filatov, S.; Egorysheva, A.; Kargin, Y. Preparation, crystal structure and thermal expansion of a new bismuth barium borate, $BaBi_2B_4O_{10}$. *J. Solid State Chem.* **2007**, *180*, 596–603. [CrossRef]

27. Burns, P.C.; Grice, J.D.; Hawthorne, F.C. Borate minerals I. Polyhedral clusters and fundamental building block. *Can. Mineral.* **1995**, *33*, 1131–1151.

28. Hawthorne, F.C. Towards a structural classification of minerals: The $^{vi}M^{iv}T2\varphi$ minerals. *Am. Mineral.* **1985**, *70*, 455–473.

29. Schindler, M.; Hawthorne, F.; Baur, W.H. A crystal-chemical approach to the composition and occurrence of vanadium minerals. *Can. Mineral.* **2000**, *38*, 1443–1456. [CrossRef]

30. Hawthorne, F.C.; Schindler, M. Understanding the weakly bonded constituents in oxusalt minerals. *Z. Für Krist.* **2008**, *223*, 41–68. [CrossRef]

31. Hawthorne, F.C. Toward theoretical mineralogy: A bond-topological approach. *Am. Mineral.* **2015**, *100*, 696–713. [CrossRef]

32. Brown, I.D.; Altermatt, D. Bond-valence parameters obtained from a systematic analysis of the Inorganic Crystal Structure Database. *Acta Crystallogr.* **1985**, *B41*, 244–247. [CrossRef]

33. Hawthorne, F.C.; Burns, P.C.; Grice, J.D. The crystal chemistry of boron. *Rev. Mineral. Geochem.* **1996**, *33*, 41–116. [CrossRef]

34. Sueno, S.; Clark, J.R.; Papike, J.J.; Konnert, J.A. Crystal-structure refinement of cubic boracite. *Am. Mineral.* **1973**, *58*, 691–697.

35. Shannon, R.D. Revised effective ionic radii and systematic studies of interatomic distances in halides and chalcogenides. *Acta Crystallogr.* **1976**, *A32*, 751–767. [CrossRef]

36. Denisov, V.N.; Ivlev, A.N.; Lipin, A.S.; Mavrin, B.N.; Orlov, V. Raman spectra and lattice dynamics of single-crystal α-Bi_2O_3. *J. Phys. Condens. Matter* **1997**, *9*, 4967–4978. [CrossRef]

37. Dogra, M.; Singh, K.; Kaur, K.; Anand, V.; Kaur, P.; Singh, P.; Bajwa, B. Investigation of gamma ray shielding, structural and dissolution rate properties of Bi_2O_3–BaO–B_2O_3–Na_2O glass system. *Radiat. Phys. Chem.* **2018**, *144*, 171–179. [CrossRef]

38. Dexter, D.L. A Theory of Sensitized Luminescence in Solids. *J. Chem. Phys.* **1953**, *21*, 836–850. [CrossRef]

39. Blasse, G. Luminescence of inorganic solids: From isolated centres to concentrated systems. *Prog. Solid State Chem.* **1988**, *18*, 79–171. [CrossRef]
40. van Shaik, W.; van Heek, M.M.E.; Middel, W.; Blasse, G. Luminescence and energy migration in a one-dimensional Gd^{3+} compound: $Ca_4GdO(BO_3)_3$. *J. Lumin.* **1995**, *63*, 103–115. [CrossRef]
41. Blasse, G. Energy transfer in oxidic phosphors. *Phys. Lett. A* **1968**, *28*, 444–445. [CrossRef]